PHYSICAL REVIEW D **89,** 113001 (2014)

Triphoton production at hadron colliders

John M. Campbell[*]
Fermilab, Batavia, Illinois 60510, USA

Ciaran Williams[†]
Niels Bohr International Academy and Discovery Center, The Niels Bohr Institute,
Blegdamsvej 17, DK-2100 Copenhagen Ø, Denmark

(Received 20 March 2014; published 3 June 2014)

We present next-to-leading order predictions for the production of triphoton final states at the LHC and the Tevatron. Our results include the effect of photon fragmentation for the first time and we are able to quantify the impact of different isolation prescriptions. We find that calculations accounting for fragmentation effects at leading order, and those employing a smooth cone isolation where no fragmentation contribution is required, are in reasonable agreement with one another. However, larger differences in the predicted rates arise when higher order corrections to the fragmentation functions are included. In addition we present full analytic results for the $\gamma\gamma\gamma$ and $\gamma\gamma+$ jet one-loop amplitudes. These amplitudes, which are particularly compact, may be useful to future higher-order calculations. Our results are available in the Monte Carlo code MCFM.

DOI: 10.1103/PhysRevD.89.113001 PACS numbers: 14.70.Bh

I. INTRODUCTION

The study of multiple photon production at hadron colliders has a long and rich history. Experimental analyses of isolated prompt diphotons have been undertaken for nearly thirty years [1–4]. More recent experimental studies at the Tevatron [5–8] and the LHC [9–12] have provided a wealth of precision data to compare with theoretical predictions. At hadron colliders, prompt photons are primarily produced through the $\mathcal{O}(\alpha_s\alpha)$ direct photon process, $h_1 + h_2 \to \gamma +$ jet. Experimentally, this high-rate process plays a special role in the calibration of jet energies and uncertainties by leveraging the simple kinematics of this process to relate the well-measured photon to the less-understood recoiling jet. The production of photon pairs, $h_1 + h_2 \to \gamma\gamma$, occurs at a much smaller rate due to the overall coupling involved, $\mathcal{O}(\alpha^2)$. However, a detailed understanding of this channel is particularly desirable in light of the recent discovery of a Higgs boson [13,14] that decays through the loop-induced process $H \to \gamma\gamma$. With the accumulation of larger data sets it should be possible to study more complex final states that include additional hadronic jets, for instance the $\mathcal{O}(\alpha_s^2\alpha)$ process $h_1 + h_2 \to \gamma + 2$ jets or the $\mathcal{O}(\alpha_s\alpha^2)$ process $h_1 + h_2 \to \gamma\gamma +$ jet. Even the relatively rare triphoton process, $h_1 + h_2 \to \gamma\gamma\gamma$ should be accessible with existing data sets. Since such processes allow a much wider range of kinematic regions, compared to simpler $2 \to 2$ reactions, one might expect their study to provide a more thorough test of the theoretical predictions.

Experimentally, photons are identified as isolated—i.e., they should be accompanied by little hadronic energy—in order to distinguish them from photons produced through other mechanisms, e.g., from neutral pion decays. On the theoretical side it has become common to treat the issue of isolation in one of two ways. The traditional approach, which implements a parton-level equivalent of an experimental isolation cut [15], requires the introduction of fragmentation functions that describe the splitting of a parton into a photon. These functions require nonperturbative input in a similar fashion to parton distribution functions (PDFs) and several sets are available that have been tuned to data from the LEP experiments [16,17]. An alternative approach [18] has been advocated which changes the isolation prescription in such a way that fragmentation functions are not required. This prescription, which has become known as "smooth cone" isolation, thus enables a more straightforward calculation of higher-order theoretical predictions for photon processes.

Theoretical predictions for the production of direct photons and photon pairs have been available at next-to-leading order (NLO) for some time [15,19]. More recently the next-to-next-to leading order (NNLO) corrections to the diphoton process have been computed using the smooth cone prescription [20]. Including the NNLO corrections increases the agreement between theory and data substantially, in particular for observables that are nontrivial for the first time at NLO, such as the azimuthal angle between the photons. Results for the production of diphotons plus one jet were considered in [21], using smooth cone isolation, and extended to account for fragmentation effects in

---

[*] johnmc@fnal.gov
[†] ciaran@nbi.dk

Ref. [22]. Smooth cone results for diphoton production in association with two jets, an important background for Higgs boson production through vector boson fusion, have also been presented recently [23–26].

In this paper we concentrate on the $\gamma\gamma\gamma$ signature, i.e. triphoton production, and use it to quantify the differences between the various isolation prescriptions. Since, even at lowest order, it contains three particles in the final state, it has a much richer kinematic structure than the simplest direct photon and diphoton processes discussed above. As a result we expect it to provide a clearer comparison of isolation effects. Since triphoton production is suppressed by a power of the electromagnetic coupling α compared to the diphoton process, the rates are much smaller and, to date, no experimental analysis has observed this signature. Despite this, with typical LHC cuts, it has the largest cross section of the triple vector boson processes that are now beginning to be probed at the LHC [27,28].

Next-to-leading order predictions, implementing smooth cone isolation, have been presented in Ref. [29]. In this paper we will present a recalculation of this process, using compact expressions for the underlying matrix elements, and extend the previous treatment to allow for the inclusion of fragmentation effects. For comparison we also present results for a similar process, $\gamma\gamma +$ jet production. Although this final state is quite similar to triphoton production it allows us to investigate whether the presence of a parton at leading order leads to qualitatively different behavior of the isolation algorithms.

This paper proceeds as follows. A summary of the NLO calculations performed in order to produce the results in this paper is given in Sec. II, including compact analytic results for the $\gamma\gamma\gamma$ one-loop amplitude. In Sec. III we discuss the various forms of isolation employed in theoretical calculations and experimental analyses. In Sec. IV we present a comparison between the different isolation prescriptions, primarily for the case of triphoton production, but also for $\gamma\gamma +$ jet production. We study triphoton phenomenology for the LHC and the Tevatron in Sec. V. Finally, we present our compact results for the $\gamma\gamma +$ jet virtual amplitudes in the Appendix.

II. CALCULATION

In this paper we present NLO calculations of the processes, $p + p \to \gamma\gamma\gamma$ and $p + p \to \gamma\gamma +$ jet. Although results for the one-loop virtual corrections to photon processes have previously been presented in Ref. [30], in that case they were obtained by forming appropriate symmetric combinations of multiparton QCD amplitudes such that gluons are effectively replaced by photons. Using this procedure one can use the $q\bar{q}ggg$ results presented in Ref. [31] to obtain photon amplitudes. However, a numerical application of this procedure is both inefficient and prone to additional numerical instability. For example, the singularities associated with non-Abelian diagrams are not present in multiphoton amplitudes, but this is only made apparent through large numerical cancellations. For this reason, we have recomputed the one-loop amplitudes using analytic unitarity methods [32–35], and the program S@M [36], in order to produce results that are as compact as possible. We believe that these analytic formulas may be useful in the future, for instance to optimize NNLO calculations of the diphoton process.

In this section we will present the one-loop amplitudes for the process,

$$0 \to \bar{q}(p_1) + q(p_2) + \gamma(p_3) + \gamma(p_4) + \gamma(p_5), \qquad (1)$$

where all momenta are outgoing and the momentum labels for the particles are given in parentheses. The tree-level amplitude is written as,

$$\begin{aligned} &A^{(0)}(1_{\bar{q}}^{h_1}, 2_q^{h_2}, 3_\gamma^{h_3}, 4_\gamma^{h_4}, 5_\gamma^{h_5}) \\ &\quad = i(\sqrt{2}eQ_i)^3 \mathcal{A}^{(0)}(1_{\bar{q}}^{h_1}, 2_q^{h_2}, 3_\gamma^{h_3}, 4_\gamma^{h_4}, 5_\gamma^{h_5}), \end{aligned} \qquad (2)$$

where the helicities of the particles are denoted by $h_1, \ldots, h_5$. Amplitudes with identical photon helicities vanish. As a result there is only one independent amplitude,

$$\mathcal{A}^{(0)}(1_{\bar{q}}^-, 2_q^+, 3_\gamma^+, 4_\gamma^+, 5_\gamma^-) = \frac{\langle 12\rangle\langle 15\rangle^2}{\langle 13\rangle\langle 14\rangle\langle 23\rangle\langle 24\rangle}, \qquad (3)$$

which corresponds to the maximally helicity violating (MHV) case. The remaining helicity amplitudes can be obtained through conjugation and line-reversal symmetries.

The one-loop amplitude can be decomposed as follows,

$$\begin{aligned} &A^{(1)}(1_{\bar{q}}^{h_1}, 2_q^{h_2}, 3_\gamma^{h_3}, 4_\gamma^{h_4}, 5_\gamma^{h_5}) \\ &\quad = \frac{\alpha_s}{2\pi}\left(\frac{N_c^2 - 1}{N_c}\right) i(\sqrt{2}eQ_i)^3 \mathcal{A}^{(1)}(1_{\bar{q}}^{h_1}, 2_q^{h_2}, 3_\gamma^{h_3}, 4_\gamma^{h_4}, 5_\gamma^{h_5}), \end{aligned} \qquad (4)$$

in terms of the virtual MHV primitive amplitude which is given by,

$$
\begin{aligned}
\mathcal{A}^{(1)}(1_q^-,2_{\bar{q}}^+,3_\gamma^+,4_\gamma^+,5_\gamma^-) = {} & \left[-\frac{1}{\epsilon^2}\left(\frac{\mu^2}{-s_{12}}\right)^{\epsilon} - \frac{3}{2\epsilon}\left(\frac{\mu^2}{-s_{25}}\right)^{\epsilon} - 3\right]\mathcal{A}^{(0)}(1_q^-,2_{\bar{q}}^+,3_\gamma^+,4_\gamma^+,5_\gamma^-) \\
& + \frac{\langle 13\rangle^3\langle 24\rangle\langle 45\rangle^2 - \langle 14\rangle^3\langle 23\rangle\langle 35\rangle^2}{\langle 13\rangle\langle 14\rangle\langle 23\rangle\langle 24\rangle\langle 34\rangle^3}\mathrm{Ls}_{-1}(s_{12};s_{35},s_{45}) - \frac{\langle 12\rangle^2\langle 45\rangle^2}{\langle 13\rangle\langle 24\rangle^3\langle 34\rangle}\mathrm{Ls}_{-1}(s_{13};s_{45},s_{25}) \\
& + \frac{\langle 12\rangle^2\langle 35\rangle^2}{\langle 14\rangle\langle 23\rangle^3\langle 34\rangle}\mathrm{Ls}_{-1}(s_{14};s_{35},s_{25}) + \frac{\langle 15\rangle^2}{\langle 14\rangle\langle 23\rangle\langle 34\rangle}\mathrm{Ls}_{-1}(s_{23};s_{45},s_{15}) \\
& - \frac{\langle 15\rangle^2}{\langle 13\rangle\langle 24\rangle\langle 34\rangle}\mathrm{Ls}_{-1}(s_{24};s_{35},s_{15}) - \frac{\langle 12\rangle^2\langle 35\rangle^2}{\langle 13\rangle\langle 23\rangle^2\langle 24\rangle\langle 34\rangle}\mathrm{Ls}_{-1}(s_{45};s_{13},s_{12}) \\
& + \frac{\langle 12\rangle^2\langle 45\rangle^2}{\langle 14\rangle\langle 24\rangle^2\langle 23\rangle\langle 34\rangle}\mathrm{Ls}_{-1}(s_{35};s_{14},s_{12}) - \frac{\langle 15\rangle^2}{\langle 24\rangle\langle 13\rangle\langle 34\rangle}\mathrm{Ls}_{-1}(s_{35};s_{12},s_{24}) \\
& + \frac{\langle 15\rangle^2}{\langle 23\rangle\langle 14\rangle\langle 34\rangle}\mathrm{Ls}_{-1}(s_{45};s_{12},s_{23}) - \frac{\langle 12\rangle\langle 25\rangle^2[32]}{\langle 23\rangle\langle 24\rangle^2}\frac{L_0(-s_{13},-s_{45})}{s_{45}} \\
& - \frac{\langle 12\rangle\langle 25\rangle^2[42]}{\langle 24\rangle\langle 23\rangle^2}\frac{L_0(-s_{14},-s_{35})}{s_{35}} + \frac{\langle 12\rangle\langle 45\rangle^2[43]}{\langle 24\rangle^2\langle 34\rangle}\frac{L_0(-s_{13},-s_{25})}{s_{25}} \\
& + \frac{\langle 13\rangle\langle 45\rangle^2[43]^2}{2\langle 24\rangle\langle 34\rangle}\frac{L_1(-s_{13},-s_{25})}{s_{25}^2} + \frac{\langle 12\rangle\langle 35\rangle^2[43]}{\langle 23\rangle^2\langle 34\rangle}\frac{L_0(-s_{14},-s_{25})}{s_{25}} \\
& - \frac{\langle 14\rangle\langle 35\rangle^2[43]^2}{2\langle 23\rangle\langle 34\rangle}\frac{L_1(-s_{14},-s_{25})}{s_{25}^2} - \frac{\langle 12\rangle\langle 15\rangle\langle 25\rangle}{\langle 13\rangle\langle 23\rangle\langle 24\rangle^2}\log\left(\frac{s_{45}}{s_{25}}\right) \\
& - \frac{\langle 12\rangle\langle 15\rangle\langle 25\rangle}{\langle 14\rangle\langle 24\rangle\langle 23\rangle^2}\log\left(\frac{s_{35}}{s_{25}}\right) + \frac{[34]}{2[25]}\left[\frac{\langle 15\rangle}{\langle 25\rangle\langle 34\rangle}\left(\frac{\langle 35\rangle}{\langle 23\rangle} + \frac{\langle 45\rangle}{\langle 24\rangle}\right) + \frac{1}{[15]}\left(\frac{[23]}{\langle 24\rangle} - \frac{[24]}{\langle 23\rangle}\right)\right]. \qquad (5)
\end{aligned}
$$

The amplitude is written in terms of the integral functions Ls_{-1}, L_0 and L_1 that are defined by,

$$
\begin{aligned}
\mathrm{Ls}_{-1}(x;y,z) = {} & \mathrm{Li}_2\left(1-\frac{y}{x}\right) + \mathrm{Li}_2\left(1-\frac{z}{x}\right) \\
& + \log\frac{y}{x}\log\frac{z}{x} - \frac{\pi^2}{6} \qquad (6)
\end{aligned}
$$

$$L_0(x,y) = \frac{\log(x/y)}{1-x/y} \qquad (7)$$

$$L_1(x,y) = \frac{L_0(x,y)+1}{1-x/y}. \qquad (8)$$

The amplitudes for $\gamma\gamma$ + jet production are presented in the Appendix.

The contribution of real radiation diagrams is straightforward and compact results have already been given in Ref. [30]. The amplitudes have been implemented in the Monte Carlo program MCFM [37–39], which handles the cancellation of singularities using Catani-Seymour dipole subtraction [40]. These calculations will be available in v6.8 of the MCFM code. For the case of triphoton production we have checked the validity of our results by finding excellent agreement with the smooth cone isolation result that may be obtained from the VBFNLO code [29]. We defer our discussion of the comparison with existing results for diphoton + jet production to Sec. IV.

III. PHOTON ISOLATION AND FRAGMENTATION

Experimental searches for prompt photons, those which participate in the hard scattering process, are complicated by the presence of secondary photons and photons arising from fragmentation processes. Secondary photons are those resulting from the decays of unstable particles (for instance $\pi^0 \to \gamma\gamma$), whilst fragmentation photons are produced from the splitting of a QCD parton. Both of these types of photons are typically accompanied by hadronic energy and thus can be suppressed by the application of isolation cuts.

For this reason experimental analyses typically apply fairly strict isolation criteria to photon candidates. The isolation region is defined by a cone of radius $R_0 = \sqrt{\Delta\phi^2 + \Delta\eta^2}$ around the photon, where $\Delta\phi$ and $\Delta\eta$ refer to the difference in azimuthal angle and pseudorapidity from the photon, respectively. One definition of the isolation requirement is to demand that the sum of the hadronic energy in the transverse direction inside this cone is less than some fixed value $E_T^{\max}$,

$$\sum_{\mathrm{had}\in R_0} E_T^{\mathrm{had}} < E_T^{\max}. \qquad (9)$$

Throughout this paper, when such a cut is applied we will refer to the procedure as "fixed energy" isolation. At the LHC, typical values for $E_T^{\max}$ range from 5–50 GeV.

An alternative strategy is to require that the total hadronic energy is less than some fixed fraction of the photon transverse momentum ϵ_γ,

$$\sum_{\mathrm{had}\in R_0} E_T^{\mathrm{had}} < \epsilon_\gamma p_T^\gamma. \tag{10}$$

This will be referred to as "fractional energy" isolation. For analyses involving energetic photons such a prescription may be more desirable since high-p_T photons can be accepted even if they are accompanied by hadronic activity that exceeds a fixed threshold chosen for more typical, softer photons.

Obtaining theoretical predictions for final states that include photons also requires particular care. At LO a process involving a fixed number of photons and jets is rendered finite by the cuts needed to define the final state objects, provided, for example, one defines a jet-photon separation minimum. However, at NLO matters are complicated by the collinear singularity associated with a quark-photon splitting. The singularity cannot be removed in a theoretically safe manner by simply applying a parton-photon separation requirement, since this cut would remove a slice of soft gluon phase space and spoil the cancellation of infrared singularities. In order to produce a finite cross section one must absorb the collinear singularity into a fragmentation function, in an analogous manner to the mass factorization of the initial state collinear singularities into the PDFs. In order to estimate the nonperturbative boundary conditions one must extract the fragmentation function from a fit to data. We shall use fragmentation functions that have been obtained by fitting data from the LEP experiments, that correspond to the results of Ref. [16] ("BFG") and Ref. [17] ("GdRG").

An alternative procedure that does not require the introduction of fragmentation functions is the isolation prescription of Frixione [18], often referred to as "smooth cone" isolation. This requires that the hadronic energy in the vicinity of the photon satisfies the following condition,

$$\sum_{\mathrm{had}} E_T^{\mathrm{had}} \theta(R - R_{\mathrm{had},\gamma}) < \epsilon_\gamma p_T^\gamma \left(\frac{1-\cos R}{1-\cos R_0}\right)^n \quad \text{for all } R \le R_0. \tag{11}$$

Using this isolation prescription it is clear that the collinear pole is removed, but that arbitrarily soft emissions are retained, thus preserving the required cancellation of singularities. Given its simplicity this type of isolation is widely used in theoretical calculations. However, due to the discrete nature of the calorimeter cells in experimental detectors, this type of isolation is difficult to impose experimentally. Recently the possibility of combining the two approaches, by using a series of staggered cones has been studied in Ref. [41].

IV. COMPARISON BETWEEN ISOLATION PROCEDURES

A. Isolation effects in $\gamma\gamma\gamma$ production

In this section we investigate the impact of the isolation prescription on predictions for triphoton production. Specifically, we will compare predictions obtained using the fixed energy, fractional energy and smooth cone isolation procedures that are defined by Eqs. (9), (10) and (11), respectively. Throughout this paper we will use the customary choice $n = 1$ in Eq. (11). For the sake of this comparison we compute NLO cross sections for the LHC operating at 14 TeV, using the default MCFM electroweak parameters that correspond in particular to $\alpha = 1/132.338$. We use the CT10 PDF set [42] and set the renormalization, factorization and fragmentation scales to be the invariant mass of the photonic system $\mu = m_{\gamma\gamma\gamma}$. The final state is defined by a basic set of cuts on the photons,

$$p_T^\gamma > 30~\mathrm{GeV}, \qquad |\eta_\gamma| < 2.5, \qquad R_{\gamma\gamma} > 0.4. \tag{12}$$

For the fixed and fractional energy isolation procedures, the calculation also depends on the choice of fragmentation functions. We consider three such sets here. The first two sets, obtained by Gehrmann-de-Ridder and Glover (GdRG) [17], correspond to strictly fixed-order extractions at $\mathcal{O}(\alpha)$ (LO) and $\mathcal{O}(\alpha\alpha_s)$ (NLO). The final set (BFG) includes a resummation of $\mathcal{O}(\alpha_s^n \log^{n+1}\mu_F^2)$ corrections and corresponds to set II of Ref. [16].

In Fig. 1 we compare the NLO cross sections for fractional and smooth cone isolation as a function of the parameter ϵ_γ that is common to both algorithms. We consider two different choices of isolation cone size, $R_0 = 0.4$ and $R_0 = 0.7$. We first note that the LO prediction does not depend on the isolation procedure and, using the appropriate LO PDF set (CTEQ6L1), the LO cross section is 6.90 fb. Regardless of the form of isolation used in the NLO calculation, the correction to the LO rate is around a factor of two or more. However it is clear that the cross section is quite sensitive to the value of ϵ_γ. This sensitivity is easily understood from the nature of the final state. Since this process proceeds only through quark-antiquark initial states at tree level, the effect of the NLO corrections is especially important due to the large gluon flux at the 14 TeV LHC. Contributions of this nature, for example real radiation channels such as $qg \to \gamma\gamma\gamma q$, are the most sensitive to the fragmentation functions and isolation definition due to the presence of a quark in the final state.

It is also clear from Fig. 1 that the predictions are rather sensitive to the fragmentation functions that are employed. The results for the LO GdRG set agree reasonably well with those using the smooth cone isolation. For the smaller cone choice these two predictions differ by around 5%, while for $R_0 = 0.7$ some differences at the 10% level are observed for the largest values of ϵ_γ. In contrast, the results obtained

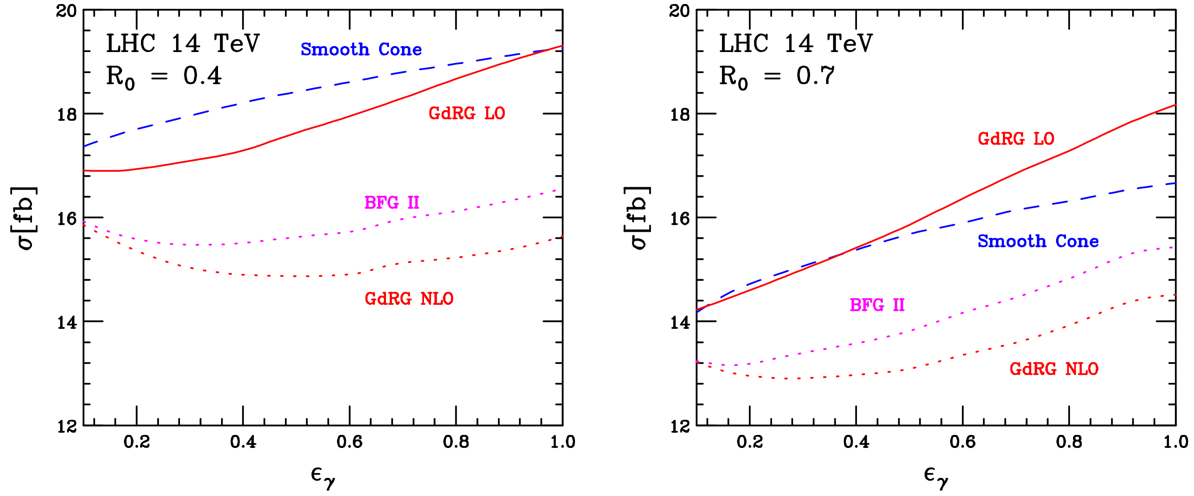

FIG. 1 (color online). Dependence of the NLO triphoton cross section on the parameter that controls the amount of hadronic energy inside the isolation cone, ϵ_γ. Results are shown for the fractional and smooth cone isolation procedures, using an isolation cone of size $R_0 = 0.4$ (left) and $R_0 = 0.7$ (right). Smooth cone predictions correspond to the dashed line, while the solid line represents the LO GdRG prediction and the dotted lines correspond to the BFG (magenta) and NLO GdRG (red) fragmentation sets.

using the NLO set of GdRG and the BFG set II are consistently 5%–10% smaller than the results for LO GdRG.[1] We note though that the predictions obtained using these sets are less sensitive to the isolation parameter ϵ_γ and the two sets yield very similar predictions for tightly isolated photons, $\epsilon_\gamma \lesssim 0.2$.

Since, in our implementation, the QCD matrix elements which multiply the fragmentation contributions are $\mathcal{O}(\alpha^2\alpha_s)$, a consistent $\mathcal{O}(\alpha^3\alpha_s)$ prediction for triphoton production is only obtained when using the $\mathcal{O}(\alpha)$ LO GdRG set. This can be seen by inspecting Fig. 2, which shows the dependence of the cross section on the fragmentation scale for the three different sets of fragmentation functions using fractional isolation with $R_0 = \epsilon_\gamma = 0.4$. The cross section obtained with the LO GdRG set is independent of the fragmentation scale since all dependence on it is exactly cancelled between integrated subtraction terms and the fragmentation functions. The other two sets of fragmentation functions include higher order corrections beyond the formal accuracy of the calculation, leading to a small residual dependence on the fragmentation scale. Of course, if higher order corrections to the fragmentation process are explicitly included in the calculation (for instance, as in predictions for direct photon and photon pair production, cf. Refs. [15,19]), this dependence is alleviated by the use of corresponding higher-order fragmentation sets. The mismatch of orders in perturbation theory may explain the unusual behavior of the GdRG NLO and BFG predictions for $R_0 = 0.4$, Fig. 1(left). For these predictions, the cross section increases as ϵ_γ decreases, for $\epsilon_\gamma < 0.5$. The increase in the cross section is much more pronounced for the $\mathcal{O}(\alpha\alpha_s)$ set of GdRG. Although it is tempting to conclude from Fig. 1 that higher order corrections could be sizeable, *a priori* we do not know the effect of the remaining higher order contributions. Therefore, based on the comparison shown in Figs. 1 and 2, we advocate the use of the $\mathcal{O}(\alpha)$ fragmentation functions with our NLO predictions. In this case we observe that such

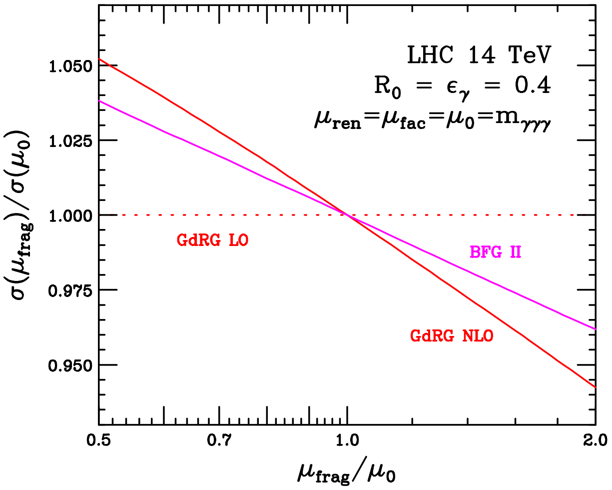

FIG. 2 (color online). Dependence of the NLO triphoton cross section on the fragmentation scale $\mu_{\rm frag}$, for the different sets of fragmentation functions. The renormalization and factorization scales are held fixed at $\mu_0 = m_{\gamma\gamma\gamma}$ while $\mu_{\rm frag}$ is varied about this central choice. The solid horizontal line represents the LO GdRG prediction and the dotted lines correspond to the BFG (magenta) and NLO GdRG (red) fragmentation sets.

---

[1] We note that the fitting range of the GdRG fragmentation sets corresponds to $\epsilon_\gamma \lesssim 0.5$ and that results may not be reliable outside this range. However, the GdRG and BFG fragmentation sets do not differ greatly in the region $\epsilon_\gamma > 0.5$. Since the BFG sets use more inclusive LEP data, this similarity gives some confidence in the GdRG set in this region.

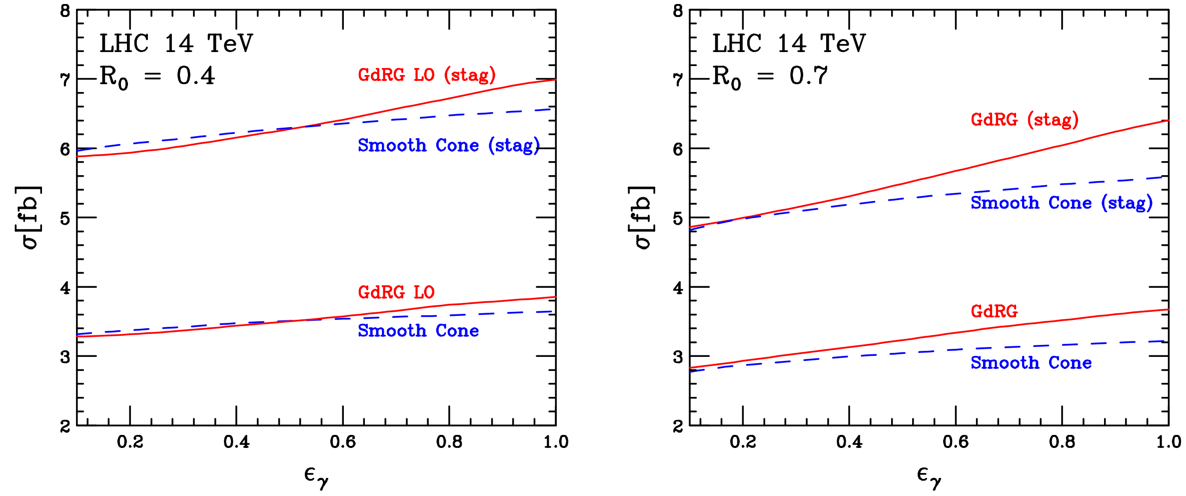

FIG. 3 (color online). Dependence of the NLO triphoton cross section on the parameter that controls the amount of hadronic energy inside the isolation cone, ϵ_γ with harder selection requirements $p_T^\gamma > 50$ GeV, and staggered cuts $p_T^\gamma > 100, 50, 30$ GeV. Results are shown for the fractional and smooth cone isolation procedures, using an isolation cone of size $R_0 = 0.4$ (left) and $R_0 = 0.7$ (right).

predictions are close to those obtained using smooth cone isolation. This suggests that, for cuts that are similar to the ones we have used here, the use of smooth cone isolation for this process should provide an adequate description of experimental isolation requirements.

Comparing the results for different cone sizes it is clear that the cross sections obtained using the larger cone size $R_0 = 0.7$ depend much more strongly on ϵ_γ. This reflects the importance of the real radiation terms on the total cross section. For large values of ϵ_γ the cross section obtained using smooth cone isolation is more strongly suppressed than for the fractional isolation. This suppression can be explained by considering event topologies in which a radiated parton is near the threshold for acceptance in the inner cone. In these topologies we assume that the radiation in the smaller cone (for example $R_0 = 0.4$) is just soft enough to pass the isolation requirement. For the fractional isolation this event will then pass all subsequent increases in cone size, since the parameters used to determine the isolation requirements are fixed (the transverse momenta of the parton and of the photon). However, for the smooth cone isolation the isolation requirements for this event change as a function of the cone size, due to the $(1 - \cos R_0)$ prefactor in Eq. (11). Therefore, as the cone size increases the smooth cone isolation requirement becomes tighter and thus more events are rejected than in the fractional isolation case.

In order to check the dependence of the isolation algorithms on the event selection cuts, we have repeated this analysis using selection criteria with higher cuts on the photon transverse momenta. Specifically, we modify the photon transverse momentum cuts of Eq. (12) as follows, with the other cuts unchanged. In the first case we simply raise the cut uniformly and require $p_T^\gamma > 50$ GeV. In the second case we use a set of cuts with staggered thresholds, $p_T^{\gamma_1} > 100$ GeV, $p_T^{\gamma_2} > 50$ GeV and $p_T^{\gamma_3} > 30$ GeV where the photons are labeled according to $p_T^{\gamma_1} > p_T^{\gamma_2} > p_T^{\gamma_3}$. Our results are shown in Fig. 3. It is clear from comparing Figs. 1 and 3 that the overall structure of the results remains the same. The smooth cone algorithm is in reasonable agreement with the fractional isolation result using the LO GdRG fragmentation functions. There is particularly good agreement for the smaller cone size of $R_0 = 0.4$, whilst more significant differences are observed for the larger

TABLE I. Triphoton cross sections at the LHC (in femtobarns), computed using the fixed energy, fractional energy and smooth cone forms of isolation prescription. The comparison uses the LO GdRG fragmentation functions and is performed for two values of the photon p_T cut.

			$R_0 = 0.4$			$R_0 = 0.7$	
Minimum p_T^γ	Isolation	$E = 5$	$E = 25$	$E = 50$	$E = 5$	$E = 25$	$E = 50$
30 GeV	fixed, $E_T^{\max} = E$ [GeV]	16.86	17.56	19.45	14.16	16.00	18.61
	fractional, $\epsilon_\gamma = E/30$	16.96	18.76	21.15	14.43	17.48	20.51
	smooth., $\epsilon_\gamma = E/30$	17.58	19.00	20.15	14.58	16.37	17.60
50 GeV	fixed, $E_T^{\max} = E$ [GeV]	3.26	3.37	3.60	2.76	3.04	3.39
	fractional, $\epsilon_\gamma = E/50$	3.28	3.50	3.86	2.83	3.23	3.68
	smooth., $\epsilon_\gamma = E/50$	3.32	3.51	3.65	2.77	3.04	3.22

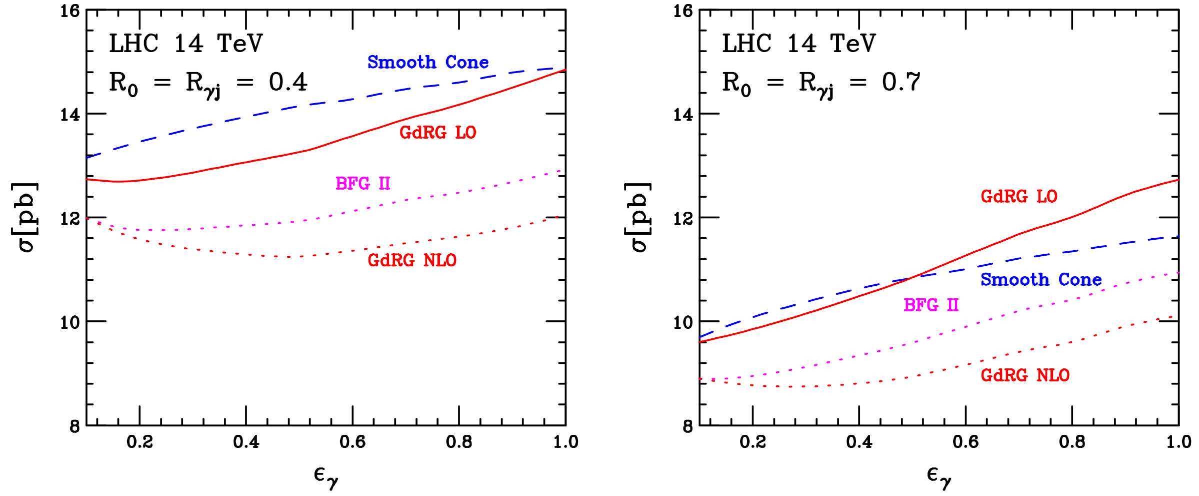

FIG. 4 (color online). Dependence of the NLO $\gamma\gamma+$jet cross section on the parameter that controls the amount of hadronic energy inside the isolation cone, ϵ_γ. Results are shown for the fractional and smooth cone isolation procedures, using an isolation cone of size $R_0=0.4$ (left) and $R_0=0.7$ (right).

cone choice and $\epsilon_\gamma>0.5$. As the photon transverse momentum cut is raised, the smooth cone results depend less strongly on ϵ_γ than those including fragmentation. This is illustrated by the fact that, for $R_0=0.4$, the GdRG prediction is smaller than the smooth cone result for $\epsilon_\gamma<0.5$ but higher for $\epsilon_\gamma>0.5$. The exact value of ϵ_γ for which the predictions intersect is of course dependent on the phase space selection requirements. For example, for the loose cuts defined previously the predictions intersected around $\epsilon_\gamma=0.95$ for $R_0=0.4$, cf. Fig. 1.

Finally we turn to the case of fixed energy isolation. In Table I we present results obtained using this form of isolation and compare them to the cross sections obtained using fractional and smooth cone isolation. Specifically, for fixed isolation with a maximum transverse energy $E_T^{\rm max}$ in Eq. (9), we compare to fractional and smooth cone isolation with $\epsilon_\gamma=E_T^{\rm max}/p^\gamma_{T,\rm min}$ in Eq. (10). When the isolation is tight ($E=5$ in Table I), the results obtained in the different cases are in very good agreement, which is simply a reflection of the fact that most of the cross section is due to production of photons near the minimum p_T threshold. However, as the isolation requirement weakens, the predictions begin to show bigger differences. Requiring a much looser criterion, $E=50$, induces differences of up to 10% for fractional and fixed isolation, with slightly smaller differences between smooth cone and fixed isolation.

B. Isolation effects in $\gamma\gamma+$jet production

As already noted, it is interesting to compare the isolation effects in $\gamma\gamma\gamma$ and $\gamma\gamma+$jet processes. In order to maximize the similarities with the triphoton results that have just been presented, for the $\gamma\gamma+$jet final state we adopt the same photon cuts as in Eq. (12) and tailor the jet cuts as follows. Partons are clustered into jets using the anti-k_T algorithm with $D=0.5$ and are required to satisfy the same rapidity requirement as the photons, i.e. $|\eta_j|<2.5$. To obtain a finite cross section we must impose a minimum jet-photon separation, $R_{\gamma,j}$. For this we use the same value as for the isolation cone, namely $R_{\gamma,j}=R_0=\{0.4,0.7\}$. The common scale choice, μ, that we have used for these calculations is given by $\mu^2=m^2_{\gamma\gamma}+\sum(p^j_T)^2$.

Results for the NLO cross section as a function of ϵ_γ for $p^j_T\ p^\gamma_T>30$ GeV are shown in Fig. 4, for the two choices $R_0=0.4$ and $R_0=0.7$. The predictions for $\gamma\gamma+$jet production are very similar to the equivalent results obtained for the $\gamma\gamma\gamma$ process (cf. Fig. 1), suggesting that the dependence of the cross section on ϵ_γ is not strongly influenced by the number of photons. Instead it is governed by the kinematics of the underlying scattering.

We note that a similar study was undertaken in Ref. [22] employing selection cuts relevant for Higgs searches in the channel $H\to\gamma\gamma$. We have repeated this analysis using the results of this paper and find agreement for very tight isolation requirements but substantial differences for larger values of ϵ_γ. The qualitative behavior of our predictions is more similar to the results shown in Fig. 4, with a milder dependence of the cross section on ϵ_γ. We understand that this difference is due to an error in the implementation of the fragmentation functions in Ref. [22].[2]

C. Summary

It is clear from the results of this section that the predictions using smooth cone isolation and those using fractional isolation are in reasonable agreement with one another, provided that the fragmentation functions are

---

[2] We thank the authors of Ref. [22] for confirmation of this issue.

restricted to fixed $\mathcal{O}(\alpha)$ accuracy. The agreement is particularly good for smaller cone choices and tighter isolation requirements. For smooth cone isolation with larger cones the $(1-\cos R_0)^{-1}$ prefactor tightens the isolation, and results in larger differences between smooth cone and fractional energy isolation for the same choice of ϵ_γ. For all of the phase space selection cuts we investigated, the smooth cone results showed the mildest dependence on ϵ_γ. Therefore, varying ϵ_γ in a smooth cone calculation in order to gauge the uncertainty associated with isolation effects is not advisable. We observed that including higher order corrections to the fragmentation functions induced large differences with respect to the smooth cone and LO GdRG sets. This may be indicative of large NNLO corrections, but since they are only a partial computation no definitive statement can be made on the impact of higher order corrections.

V. RESULTS

A. Triphotons at the LHC

In this section we provide predictions for the triphoton process at the LHC, operating at a variety of center of mass energies. We use a set of basic cuts that is appropriate for experimental analyses at the LHC and which closely corresponds to the cuts used in the previous section, cf. Eq. (12). The photons are required to satisfy,

$$|\eta_\gamma| < 2.5, \qquad R_{\gamma\gamma} > 0.4, \qquad \sum_{\in R_\gamma = 0.4} E_T^{\rm had} < 0.4 p_T^\gamma, \quad (13)$$

i.e. we use the fractional form of isolation and, following the conclusions of our previous analysis, the LO GdRG set of fragmentation functions. As before we employ the CT10 (CTEQ6L1) PDF set for our NLO (LO) predictions. We consider two thresholds for the photon transverse momenta, $p_T^\gamma > 30$ GeV and $p_T^\gamma > 50$ GeV. Our results for the two values of the cut are collected in Table II.

TABLE II. Summary of LHC triphoton cross sections at various LHC operating energies, with two choices of photon p_T threshold.

$\sqrt{s}$	Photon cut	LO [fb]	NLO [fb]	K-factor
7 TeV	$p_T^\gamma > 30$ GeV	$3.36^{+1\%}_{-2\%}$	$7.49^{+6\%}_{-4\%}$	2.23
	$p_T^\gamma > 50$ GeV	$0.64^{+2\%}_{-1\%}$	$1.30^{+6\%}_{-5\%}$	2.03
8 TeV	$p_T^\gamma > 30$ GeV	$3.89^{+2\%}_{-3\%}$	$8.87^{+5\%}_{-5\%}$	2.28
	$p_T^\gamma > 50$ GeV	$0.77^{+1\%}_{-1\%}$	$1.60^{+6\%}_{-4\%}$	2.08
13 TeV	$p_T^\gamma > 30$ GeV	$6.42^{+4\%}_{-5\%}$	$15.87^{+4\%}_{-3\%}$	2.47
	$p_T^\gamma > 50$ GeV	$1.38^{+1\%}_{-1\%}$	$3.13^{+5\%}_{-4\%}$	2.27
14 TeV	$p_T^\gamma > 30$ GeV	$6.91^{+5\%}_{-6\%}$	$17.28^{+4\%}_{-3\%}$	2.50
	$p_T^\gamma > 50$ GeV	$1.50^{+1\%}_{-2\%}$	$3.44^{+5\%}_{-4\%}$	2.29

The results have been obtained using $m_{\gamma\gamma\gamma}$ as the central renormalization, factorization and fragmentation scale and the quoted uncertainty corresponds to variation of this central scale by a factor of two in each direction. Since this process does not depend on the strong coupling at leading order, there is only a very small dependence on the factorization scale at that order. At NLO the prediction becomes sensitive to the gluon distribution and, as a result, we observe large K-factors (∼2–2.5) when going from LO to NLO. Thus it is only at NLO that one obtains a realistic prediction for the normalization of these processes at the LHC. At NLO the scale dependence remains rather small, and reflects a partial cancellation between the factorization and renormalization scales. As $\sqrt{s}$ increases the dependence on the factorization scale increases, as can clearly be seen from the LO results, such that the cancellation becomes more complete. At 14 TeV this procedure yields a scale uncertainty of about ±4%. It should be borne in mind that other sources of uncertainty, for instance due to the particular choice of fragmentation functions, are not accounted for here. As noted in the previous section such uncertainties may be at least as large.

In Fig. 5 we present the differential distribution for the p_T of the hardest photon. This distribution is significantly altered by the higher order corrections, both in rate and shape. The region $p_T < 2p_T^{\rm min}$ experiences the most dramatic corrections. Since we require three photons with $p_T > 30$ GeV, this distribution has a distinct broad peak around 60 GeV. At NLO the kinematic suppression in the region $p_T < 60$ GeV is reduced due to the presence of real radiation contributions that allow a parton to recoil against

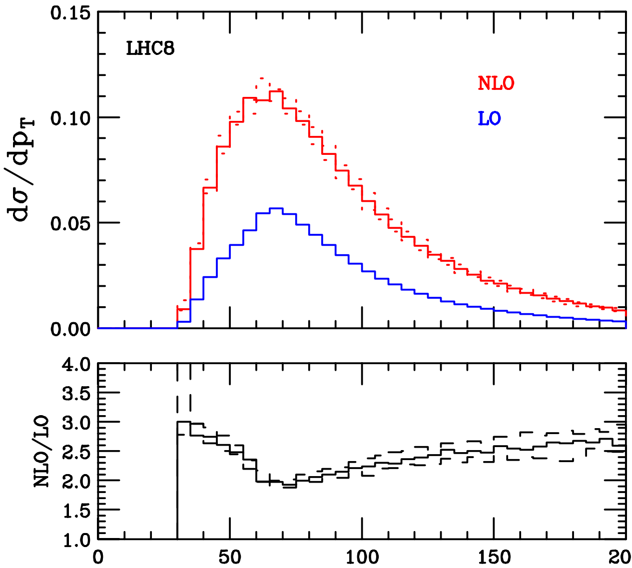

FIG. 5 (color online). The $p_{T,\gamma}$ spectrum for the hardest photon at the 8 TeV LHC. The solid lines represent the contributions with $\mu = m_{\gamma\gamma\gamma}$, the dashed lines represent the NLO predictions with $\mu = \{0.5, 2\} m_{\gamma\gamma\gamma}$.

the photonic system. This leads to the K-factor in this region being larger than at the peak of the distribution.

B. Triphotons at the Tevatron

Since the leading order triphoton process is $q\bar{q} \to \gamma\gamma\gamma$, this process is significantly easier to produce at a $p\bar{p}$ collider where both the quark and the antiquark may be described by the valence content of the proton and antiproton, respectively. This is to be contrasted with an equivalent pp machine where the antiquark must be obtained from the proton sea. For this reason it is interesting to contrast the LHC results of the previous section with the triphoton cross section at the Tevatron.

To that end we define a set of cuts that is appropriate for experimental analyses that could be performed at the Tevatron,

$$\begin{aligned} &p_T^\gamma > 15\ \text{GeV}, && |\eta_\gamma| < 1.1, \\ &R_{\gamma\gamma} > 0.4, && \sum_{\in R_\gamma = 0.4} E_T^{\text{had}} < 5\ \text{GeV} \end{aligned} \tag{14}$$

and use the same parton distribution and fragmentation functions as before. Note though that the isolation condition is now at a fixed energy rather than taking the fractional form, although since the isolation condition is rather strict it could be well described by a corresponding fractional isolation, cf. Table I. With these cuts the triphoton cross section is

$$\sigma_{\gamma\gamma\gamma}^{\text{NLO}} = 4.74^{+6\%}_{-5\%}\ [\text{fb}]. \tag{15}$$

As was the case at the LHC, the NLO corrections to this process result in a large K-factor (1.93) when comparing with the LO result of 2.46 fb (obtained using the CTEQ6L1 PDF set). The upper and lower percentages in the above result represent scale variation by a factor of two around a central scale choice of $\mu = m_{\gamma\gamma\gamma}$. Given the 10 fb^{-1} of data recorded by the CDF and D0 detectors during Run II of the Tevatron, one therefore expects $\mathcal{O}(50)$ events in the total data set, before accounting for acceptance and efficiency corrections. This suggests that a measurement of this process by the Tevatron experiments may therefore also be possible.

VI. CONCLUSIONS

In this paper we have studied the production of triphoton final states at hadron colliders, paying particular attention to the role of photon fragmentation and isolation effects. We calculated compact analytic expressions for $\gamma\gamma\gamma$ and $\gamma\gamma+\text{jet}$ one-loop amplitudes and used them to implement these processes in MCFM. We investigated the impact of different isolation prescriptions, finding that the NLO cross section is quite sensitive to the type of isolation and fragmentation functions applied. This is due to the fact that a large part of the NLO cross section arises from configurations that contain an initial state gluon and, consequently, a quark in the final state. With three photons in the final state, the phase space in which this quark is near a photon is large and therefore the NLO prediction is especially sensitive to the isolation definition. We investigated the impact of different fragmentation functions on the NLO cross section. We found that the results obtained using predictions accurate to $\mathcal{O}(\alpha^3\alpha_s)$, i.e. using smooth cone isolation and LO GdRG fragmentation contributions, are similar to each other. However, including higher order effects in the predictions for the fragmentation functions resulted in substantially different results. Since our predictions do not include the full $\mathcal{O}(\alpha_s^2)$ corrections we advocated the use of LO fragmentation sets which result in a consistent NLO prediction.

We studied the phenomenology of triphoton production at hadron colliders. We presented NLO cross sections for a range of LHC operating energies and phase space selection criteria. At 8 TeV the cross sections are typically around 5 fb, suggesting that this signal should be observable in the existing LHC data set. The measurement of this cross section would be one of the first studying triboson production. The study of this class of processes is extremely interesting since it tests the interplay between electroweak and QCD physics in a final state involving multiple electroweak couplings.

Since at LO the production of triphotons is dominated by $u\bar{u}$ initial states, $p\bar{p}$ colliders are more sensitive to this process than equivalent pp machines. Indeed the cross section at the Tevatron, with different cuts more appropriate for a lower-energy machine, is also around 5 fb. Therefore with the 10 fb^{-1} data set accumulated by the CDF and D0 experiments this signature may also be observable at the Tevatron.

Our results for $\gamma\gamma\gamma$ and $\gamma\gamma+\text{jet}$ have been implemented into MCFM v6.8, including all of the fragmentation functions studied in this paper.

ACKNOWLEDGMENTS

We thank Keith Ellis and the authors of Ref. [22] for useful discussions. The research of J. M. C. is supported by the U.S. DOE under Contract No. DE-AC02-07CH11359.

APPENDIX: AMPLITUDES FOR $\gamma\gamma$ + JET

In this appendix we present the amplitudes needed to compute the NLO corrections to $\gamma\gamma+\text{jet}$ production,

$$0 \to \bar{q}(p_1) + q(p_2) + g(p_3) + \gamma(p_4) + \gamma(p_5). \tag{A1}$$

At leading order the amplitude can be decomposed into the following color stripped amplitude,

$$A^{(0)}(1_{\bar{q}}^{h_1}, 2_q^{h_2}, 3_g^{h_3}, 4_\gamma^{h_4}, 5_\gamma^{h_5}) = 2\sqrt{2} i Q_q^2 e^2 g_s (T^{a_3}_{i_1 i_2}) \times \mathcal{A}^{(0)}(1_{\bar{q}}^{h_1}, 2_q^{h_2}, 3_g^{h_3}, 4_\gamma^{h_4}, 5_\gamma^{h_5}). \tag{A2}$$

The nonvanishing helicity amplitudes for the LO process have identical kinematic structure to Eq. (3), i.e.

$$\mathcal{A}^{(0)}(1_{\bar{q}}^-, 2_q^+, 3_g^+, 4_\gamma^+, 5_\gamma^-) = \frac{\langle 12\rangle\langle 15\rangle^2}{\langle 13\rangle\langle 14\rangle\langle 23\rangle\langle 24\rangle}, \tag{A3}$$

$$\mathcal{A}^{(0)}(1_{\bar{q}}^-, 2_q^+, 3_g^-, 4_\gamma^+, 5_\gamma^+) = \frac{\langle 12\rangle\langle 13\rangle^2}{\langle 15\rangle\langle 14\rangle\langle 25\rangle\langle 24\rangle}. \tag{A4}$$

For simplicity we refer to these helicity structures as the "γ-MHV" and "g-MHV" amplitudes, with the nomenclature denoting the identity of the negative-helicity particle. Although these amplitudes are trivially related at LO,

$$\mathcal{A}^{(0)}(1_{\bar{q}}^-, 2_q^+, 3_g^-, 4_\gamma^+, 5_\gamma^+) = \mathcal{A}^{(0)}(1_{\bar{q}}^-, 2_q^+, 5_g^+, 4_\gamma^+, 3_\gamma^-), \tag{A5}$$

differences arise in the one-loop and real radiation amplitudes. At one loop the amplitude can be decomposed into the following leading and subleading color pieces

$$A^{(1)}(1_{\bar{q}}^{h_1}, 2_q^{h_2}, 3_g^{h_3}, 4_\gamma^{h_4}, 5_\gamma^{h_5}) = N_c \frac{\alpha_s}{4\pi}(2\sqrt{2}) i e^2 g_s (T^{a_3}_{i_1 i_2}) \Bigg(Q_q^2 \mathcal{A}^{(L)}(1_{\bar{q}}^{h_1}, 2_q^{h_2}, 3_g^{h_3}, 4_\gamma^{h_4}, 5_\gamma^{h_5}) + \frac{Q_q^2}{N_c^2}\mathcal{A}^{(R)}(1_{\bar{q}}^{h_1}, 2_q^{h_2}, 3_g^{h_3}, 4_\gamma^{h_4}, 5_\gamma^{h_5}) - \sum_i \frac{Q_i^2}{N_c}\mathcal{A}^{N_f}(1_{\bar{q}}^{h_1}, 2_q^{h_2}, 3_g^{h_3}, 4_\gamma^{h_4}, 5_\gamma^{h_5}) \Bigg). \tag{A6}$$

In the above equation the summation over i represents the contributions arising from closed (light) fermion loops, which in our implementation corresponds to $i = u, d, s, c, b$. In all cases the subleading R pieces can be obtained from the $\gamma\gamma\gamma$ helicity amplitudes presented in Sec. II, i.e. $\mathcal{A}^{(R)}(1_{\bar{q}}^{h_1}, 2_q^{h_2}, 3_g^{h_3}, 4_\gamma^{h_4}, 5_\gamma^{h_5}) = \mathcal{A}^{(1)}(1_{\bar{q}}^{h_1}, 2_q^{h_2}, 3_\gamma^{h_3}, 4_\gamma^{h_4}, 5_\gamma^{h_5})$. As a result we need only present the amplitudes that appear at leading color or contain closed fermion loops.

We begin by presenting the unrenormalized γ-MHV amplitude,

$$\begin{aligned}
\mathcal{A}^{(L)}(1_q^-, 2_{\bar{q}}^+, 3_g^+, 4_\gamma^+, 5_\gamma^-) = {}& \left[\frac{1}{\epsilon^2}\left(\left(\frac{\mu^2}{-s_{13}}\right)^\epsilon + \left(\frac{\mu^2}{-s_{23}}\right)^\epsilon\right) + \frac{3}{2\epsilon}\left(\frac{\mu^2}{-s_{25}}\right)^\epsilon + 3\right]\mathcal{A}^{(0)}(1_q^-, 2_{\bar{q}}^+, 3_g^+, 4_\gamma^+, 5_\gamma^-) \\
& - \frac{\langle 12\rangle^3\langle 45\rangle^2}{\langle 13\rangle\langle 14\rangle\langle 23\rangle\langle 24\rangle^3}\mathrm{Ls}_{-1}(s_{13}; s_{45}, s_{25}) + \frac{\langle 15\rangle^2}{\langle 13\rangle\langle 24\rangle\langle 34\rangle}\mathrm{Ls}_{-1}(s_{15}; s_{24}, s_{23}) \\
& - \frac{\langle 12\rangle\langle 15\rangle^2}{\langle 13\rangle\langle 14\rangle\langle 23\rangle\langle 24\rangle}\mathrm{Ls}_{-1}(s_{23}; s_{45}, s_{15}) - \frac{\langle 13\rangle^2\langle 45\rangle^2}{\langle 14\rangle\langle 23\rangle\langle 34\rangle^3}\mathrm{Ls}_{-1}(s_{25}; s_{14}, s_{13}) \\
& - \frac{\langle 12\rangle\langle 15\rangle^2}{\langle 13\rangle\langle 14\rangle\langle 23\rangle\langle 24\rangle}\mathrm{Ls}_{-1}(s_{45}; s_{13}, s_{23}) + \frac{\langle 12\rangle\langle 25\rangle^2[32]}{\langle 23\rangle\langle 24\rangle^2}\frac{L_0(-s_{13}, -s_{45})}{s_{45}} \\
& - \frac{(\langle 13\rangle\langle 24\rangle + \langle 12\rangle\langle 34\rangle)\langle 45\rangle^2[43]}{\langle 24\rangle^2\langle 34\rangle^2}\frac{L_0(-s_{13}, -s_{25})}{s_{25}} - \frac{\langle 13\rangle\langle 45\rangle^2[43]^2}{2\langle 24\rangle\langle 34\rangle}\frac{L_1(-s_{13}, -s_{25})}{s_{25}^2} \\
& + (\langle 15\rangle\langle 34\rangle - \langle 13\rangle\langle 45\rangle)\frac{\langle 35\rangle[43]}{\langle 23\rangle\langle 34\rangle^2}\frac{L_0(-s_{14}, -s_{25})}{s_{25}} - \frac{\langle 14\rangle\langle 35\rangle^2[43]^2}{2\langle 23\rangle\langle 34\rangle}\frac{L_1(-s_{14}, -s_{25})}{s_{25}^2} \\
& + \frac{\langle 12\rangle\langle 25\rangle\langle 15\rangle}{\langle 13\rangle\langle 23\rangle\langle 24\rangle^2}\log\left(\frac{s_{45}}{s_{25}}\right) + \frac{\langle 34\rangle[34]^2}{2\langle 23\rangle\langle 24\rangle[15][25]}.
\end{aligned} \tag{A7}$$

The unrenormalized g-MHV amplitude is given by,

$$\begin{aligned}\mathcal{A}^{(L)}(1_q^-,2_{\bar{q}}^+,3_g^-,4_\gamma^+,5_\gamma^+) = {} & \left[\frac{1}{\epsilon^2}\left(\left(\frac{\mu^2}{-s_{13}}\right)^\epsilon+\left(\frac{\mu^2}{-s_{23}}\right)^\epsilon\right)+\frac{3}{2\epsilon}\left(\frac{\mu^2}{-s_{23}}\right)^\epsilon+3\right]\mathcal{A}^{(0)}(1_q^-,2_{\bar{q}}^+,3_g^-,4_\gamma^+,5_\gamma^+) \\ & +\frac{\langle 13\rangle^2}{\langle 14\rangle\langle 25\rangle\langle 45\rangle}\mathrm{Ls}_{-1}(s_{14};s_{25},s_{23})-\frac{\langle 13\rangle^2}{\langle 15\rangle\langle 24\rangle\langle 45\rangle}\mathrm{Ls}_{-1}(s_{15};s_{24},s_{23}) \\ & -\frac{\langle 13\rangle^2}{\langle 15\rangle\langle 24\rangle\langle 45\rangle}\mathrm{Ls}_{-1}(s_{24};s_{15},s_{13})+\frac{\langle 13\rangle^2}{\langle 14\rangle\langle 25\rangle\langle 45\rangle}\mathrm{Ls}_{-1}(s_{25};s_{14},s_{13}) \\ & -\frac{\langle 14\rangle\langle 35\rangle^2[54]^2}{2\langle 25\rangle\langle 45\rangle}\frac{L_1(s_{14},s_{23})}{s_{23}^2}-\frac{\langle 13\rangle\langle 35\rangle[54]}{\langle 25\rangle\langle 45\rangle}\frac{L_0(s_{14},s_{23})}{s_{23}} \\ & +\frac{\langle 15\rangle\langle 34\rangle^2[54]^2}{2\langle 24\rangle\langle 45\rangle}\frac{L_1(s_{15},s_{23})}{s_{23}^2}-\frac{\langle 13\rangle\langle 34\rangle[54]}{\langle 24\rangle\langle 45\rangle}\frac{L_0(s_{15},s_{23})}{s_{23}} \\ & -\frac{[45]}{2[13][23]}\left(\frac{[24]}{\langle 25\rangle}-\frac{[25]}{\langle 24\rangle}\right)+\frac{\langle 13\rangle[45]}{2\langle 23\rangle[23]\langle 45\rangle}\left(\frac{\langle 34\rangle}{\langle 24\rangle}+\frac{\langle 35\rangle}{\langle 25\rangle}\right). \end{aligned} \tag{A8}$$

These amplitudes must be renormalized, which is achieved by adding a UV counterterm that also accounts for the transition to the normal $\overline{\mathrm{MS}}$ definition of the strong coupling,

$$\mathcal{A}^{(L)}(1_{\bar{q}}^{h_1},2_q^{h_2},3_g^{h_3},4_\gamma^{h_4},5_\gamma^{h_5}) \to \mathcal{A}^{(L)}(1_{\bar{q}}^{h_1},2_q^{h_2},3_g^{h_3},4_\gamma^{h_4},5_\gamma^{h_5})-\frac{1}{6}\left[\frac{1}{\epsilon}\left(11-\frac{2N_f}{N_c}\right)-1\right]\mathcal{A}^{(0)}(1_{\bar{q}}^{h_1},2_q^{h_2},3_g^{h_3},4_\gamma^{h_4},5_\gamma^{h_5}). \tag{A9}$$

Finally the amplitude arising from closed loops of fermions is

$$\begin{aligned}\mathcal{A}^{N_f}(1_q^-,2_{\bar{q}}^+,3_g^+,4_\gamma^+,5_\gamma^-) = {} & -2\left(\frac{\langle 14\rangle^2\langle 35\rangle^2+\langle 13\rangle^2\langle 45\rangle^2}{\langle 12\rangle\langle 34\rangle^4}\right)\mathrm{Ls}_{-1}(s_{12};s_{35},s_{45})-\frac{\langle 14\rangle\langle 35\rangle[43]}{\langle 12\rangle\langle 34\rangle^3}(2\langle 14\rangle\langle 35\rangle+4\langle 13\rangle\langle 45\rangle) \\ & \times\frac{L_0(-s_{12},-s_{35})}{s_{35}}-2\frac{\langle 14\rangle^2\langle 35\rangle^2\langle 45\rangle[43][54]}{\langle 12\rangle\langle 34\rangle^3}\frac{L_1(-s_{12},-s_{35})}{s_{35}^2} \\ & -\frac{\langle 13\rangle\langle 45\rangle[34]}{\langle 12\rangle\langle 43\rangle^3}(2\langle 13\rangle\langle 45\rangle+4\langle 14\rangle\langle 35\rangle)\frac{L_0(-s_{12},-s_{45})}{s_{45}} \\ & -2\frac{\langle 13\rangle^2\langle 45\rangle^2\langle 35\rangle[34][53]}{\langle 12\rangle\langle 43\rangle^3}\frac{L_1(-s_{12},-s_{45})}{s_{45}^2}-\frac{2\langle 35\rangle\langle 45\rangle[25]^2[34]}{\langle 34\rangle^3[12][35][45]}. \end{aligned} \tag{A10}$$

For the fermion loops the g-MHV and γ-MHV amplitudes are related in the same manner as the leading order ones,

$$\mathcal{A}^{N_f}(1_{\bar{q}}^-,2_q^+,3_g^-,4_\gamma^+,5_\gamma^+) = \mathcal{A}^{N_f}(1_{\bar{q}}^-,2_q^+,5_g^+,4_\gamma^+,3_\gamma^-). \tag{A11}$$

---

[1] E. Bonvin *et al.* (WA70 Collaboration), Z. Phys. C **41**, 591 (1989).

[2] C. Albajar *et al.* (UA1 Collaboration), Phys. Lett. B **209**, 385 (1988).

[3] J. Alitti *et al.* (UA2 Collaboration), Phys. Lett. B **288**, 386 (1992).

[4] F. Abe *et al.* (CDF Collaboration), Phys. Rev. Lett. **70**, 2232 (1993).

[5] S. Abachi *et al.* (D0 Collaboration), Phys. Rev. Lett. **77**, 5011 (1996).

[6] T. Aaltonen *et al.* (CDF Collaboration), Phys. Rev. D **84**, 052006 (2011).

[7] V. Abazov *et al.* (D0 Collaboration), Phys. Lett. B **690**, 108 (2010).

[8] T. Aaltonen *et al.* (CDF Collaboration), Phys. Rev. Lett. **110**, 101801 (2013).

[9] S. Chatrchyan *et al.* (CMS Collaboration), J. High Energy Phys. 01 (2012) 133.

[10] G. Aad *et al.* (ATLAS Collaboration), J. High Energy Phys. 01 (2013) 086.

[11] G. Aad *et al.* (ATLAS Collaboration), Phys. Rev. D **89**, 052004 (2014).
[12] S. Chatrchyan *et al.* (CMS Collaboration), arXiv:1311.6141.
[13] G. Aad *et al.* (ATLAS Collaboration), Phys. Lett. B **716**, 1 (2012).
[14] S. Chatrchyan *et al.* (CMS Collaboration), Phys. Lett. B **716**, 30 (2012).
[15] S. Catani, M. Fontannaz, J. Guillet, and E. Pilon, J. High Energy Phys. 05 (2002) 028.
[16] L. Bourhis, M. Fontannaz, and J. Guillet, Eur. Phys. J. C **2**, 529 (1998).
[17] A. G.-De Ridder and E. N. Glover, Nucl. Phys. **B517**, 269 (1998).
[18] S. Frixione, Phys. Lett. B **429**, 369 (1998).
[19] T. Binoth, J. Guillet, E. Pilon, and M. Werlen, Eur. Phys. J. C **16**, 311 (2000).
[20] S. Catani, L. Cieri, D. de Florian, G. Ferrera, and M. Grazzini, Phys. Rev. Lett. **108**, 072001 (2012).
[21] V. D. Duca, F. Maltoni, Z. Nagy, and Z. Trocsanyi, J. High Energy Phys. 04 (2003) 059.
[22] T. Gehrmann, N. Greiner, and G. Heinrich, J. High Energy Phys. 06 (2013) 058.
[23] T. Gehrmann, N. Greiner, and G. Heinrich, Phys. Rev. Lett. **111**, 222002 (2013).
[24] Z. Bern, L. Dixon, F. F. Cordero, S. Hoeche, H. Ita *et al.*, arXiv:1312.0592.
[25] S. Badger, A. Guffanti, and V. Yundin, J. High Energy Phys. 03 (2014) 122.
[26] Z. Bern, L. Dixon, F. F. Cordero, S. Hoeche, H. Ita *et al.*, arXiv:1402.4127.
[27] G. Aad *et al.* (ATLAS Collaboration), Report No. ATL-PHYS-PUB-2013-006, 2013.
[28] S. Chatrchyan *et al.* (CMS Collaboration), Report No. CMS-PAS-SMP-13-009, 2013.
[29] G. Bozzi, F. Campanario, M. Rauch, and D. Zeppenfeld, Phys. Rev. D **84**, 074028 (2011).
[30] V. D. Duca, W. B. Kilgore, and F. Maltoni, Nucl. Phys. **B566**, 252 (2000).
[31] Z. Bern, L. J. Dixon, and D. A. Kosower, Nucl. Phys. **B437**, 259 (1995).
[32] R. Britto, F. Cachazo, and B. Feng, Nucl. Phys. **B725**, 275 (2005).
[33] R. Britto, B. Feng, and P. Mastrolia, Phys. Rev. D **73**, 105004 (2006).
[34] P. Mastrolia, Phys. Lett. B **678**, 246 (2009).
[35] S. Badger, J. High Energy Phys. 01 (2009) 049.
[36] D. Maitre and P. Mastrolia, Comput. Phys. Commun. **179**, 501 (2008).
[37] J. M. Campbell and R. K. Ellis, Phys. Rev. D **60**, 113006 (1999).
[38] J. M. Campbell, R. K. Ellis, and C. Williams, J. High Energy Phys. 07 (2011) 018.
[39] J. M. Campbell, R. K. Ellis, and C. Williams, http://mcfm.fnal.gov.
[40] S. Catani and M. Seymour, Nucl. Phys. **B485**, 291 (1997).
[41] S. Catani, M. Fontannaz, J. P. Guillet, and E. Pilon, J. High Energy Phys. 09 (2013) 007.
[42] H.-L. Lai, M. Guzzi, J. Huston, Z. Li, P. M. Nadolsky, J. Pumplin, and C.-P. Yuan, Phys. Rev. D **82**, 074024 (2010).